STATISTICAL ANALYSIS OF FACTORS AFFECTING THE FLOW CHARACTERISTICS AND THERMAL EFFICIENCY OF A BUILDING INTEGRATED THERMAL (BIT) SOLAR COLLECTOR

Faisal Ghani[1] and Mike Duke[2]

[1] Solimpeks Australia, Sydney, New South Wales (Australia)

[2] Department of Engineering, the University of Waikato, Hamilton (New Zealand)

Abstract

Previous research has identified four factors (array geometry, manifold to riser channel ratio, flow direction in manifold, and the mass flow rate) which will influence the distribution of internal fluid flow within a solar thermal collector. In this study, a two level full factorial (2^k) experiment was designed in order to statistically rank their impact and also to identify any significant interactions between these factors. The thermal efficiency of the array, calculated by means of a fluid and heat transfer analysis was taken to be the experiment response. During the heat transfer analysis we approximated the fin efficiency of a BIT collector using the finite difference method which considered the heat losses through the structural ribs of the collector. A statistical analysis of the results revealed that all four main effects had a statistical influence on thermal efficiency of the array at 5 per cent significance level. The main effects ranked from highest to lowest in impact were found to be; geometry, manifold to riser fluid channel diameter, mass flow rate, and the direction of flow in the manifolds. Additionally, two secondary interactions were found to have a statistical influence on the experiment response; the array geometry and the direction of flow in the manifold followed by the array geometry and the ratio of manifold to fluid channel diameter. As the geometry of the BIT collector will vary from customer to customer due to its custom nature, these results indicate that the design of a BIT system should consider the effects of flow distribution. Finally, our numerical analysis of the fin efficiency revealed an approximate 5% drop due to additional heat losses through the structural ribs.

Keywords: Building integrated, solar thermal, flow distribution, finite difference.

1. Introduction

Conversion of solar energy is an attractive alternative to the use of fossil fuels. By harnessing the essentially inexhaustible supply of energy from the sun, we are able to reduce our dependence on fossil fuels and consequently the production of harmful carbon emissions. In addition to growing environmental concerns, seeking alternatives to oil, the supply of which is forecast to diminish significantly in the near future is also of interest to national security. Countries such as China, India, UK, and the USA are all net importers of energy and are heavily dependent on fuel imports (Asif, M. and Muneer, T. 2007). Consequently, global effort is searching for means to enhance this field from both a technological and economic perspective.

A number of methods currently exist in order to convert solar radiation into useful forms of energy such as heat and electricity. In this work, however, we are only concerned with the conversion of solar energy into thermal energy. Solar thermal technology has an extensive history where it has been primarily used for hot water and space heating applications. As hot water heating represents a significant portion of the typical household's electricity consumption, the implementation of solar thermal collectors saw double digit annual growth in Australia and New Zealand over the 2008/2009 period (Weiss, W. and Mauthner, F. 2012). Further adoption of this technology can be expected by the further reduction of system cost.

A low-cost building integrated type solar thermal collector (Figure 1) henceforth referred to as a BIT collector is currently under development at the University of Waikato. Cost reductions with this collector type are achieved by replacing standard building components with solar conversion materials thereby reducing both material and installation redundancies (Corbin, C. and Zhiqiang, J.Z. 2010). The unglazed BIT collector is suitable for various low temperature applications such as pool heating which requires a low cost solution or for pre-heating domestic hot water systems (Zhai, X.Q., Wang, R.Z., et al. 2007). Although an unglazed collector will suffer high top heat losses, the absence of a cover and therefore its associated reflection losses results in a higher thermal offset efficiency (when $T_{fluid} = T_{absorber}$) making it ideal for low temperature purposes.

An unglazed building integrated thermal collector fabricated from galvanised and painted sheet metal was investigated by a group in Slovenia (Medved, S., Arkar, C., et al. 2003). This combined numerical and

experimental study demonstrated that the unglazed building integrated thermal collector has substantial economic benefit over conventional glazed solar thermal collectors for low temperature applications. The numerical analysis carried out however in this work makes the assumption that flow within each of the fluid risers is uniform. Several studies have shown this is not the case for practical installations.
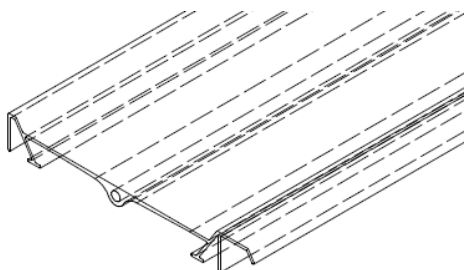

Fig. 1: Drawing of BIT concept collector under development at the University of Waikato.

An early numerical study was carried out to investigate the effect of non-uniform flow within a solar thermal collector (Chiou, J.P. 1982). Sixteen artificially assumed models were used to demonstrate the correlation between the deterioration of thermal performance and flow uniformity. It was found in this study that the thermal efficiency deteriorated between 2 and 20 per cent for the flow scenarios investigated.

Another study also showed that the thermal performance of an array of solar thermal collectors will be influenced by distribution of coolant flow (Wang, S.A. and Wu, L.G. 1990). A combined numerical and experimental study was performed on the array of 10 series connected solar thermal collectors operating under parallel and reverse flow in the manifolds. For the case of parallel flow, fluid channel flow rates were found to be greatest near the inlet and outlet ports with little flow registered by the central risers. Consequently collectors near the inlet and outlet ports were substantially cooler than collectors located about the array centre. The pattern of flow distribution was different for the case of reverse flow in the manifolds. For this scenario, it was found that flow was greatest for fluid risers near the inlet/outlet port with a non-linear drop for the proceeding fluid risers. Such a flow pattern meant that the first few collectors operated substantially cooler than the remaining array. Similar results were obtained by the authors in an earlier study (Ghani, F., Duke, M., et al. 2012). As the array operating under parallel flow was determined to operate with an average thermal efficiency 15% higher than the array operating under reverse flow, the authors recommended avoiding this fluid scheme.

In addition to the direction of flow in the manifolds examined in the previous study Jones and Lior (Jones, G.F. and Lior, N.L. 1994) examined other parameters and their effect on flow distribution. In their numerical study, the ratio of the manifold and fluid riser diameters, the number of risers, and the length of the risers were identified to have a significant influence on the flow distribution. Flow distribution was found to worsen if the ratio of the manifold to riser diameters and the riser length reduced and the number of fluid risers increased.

Research conducted so far into the effect of flow distribution has been largely limited to traditional solar thermal technology. In this study, however, we investigate this issue further by examining the effects of array geometry, the manifold to riser diameter ratio, direction of flow in the manifold, and the mass flow rate on a BIT collector. A numerical approach is outlined in the proceeding sections where the fluid channels flow rates are quantified by carrying out a fluid analysis in a commercial FEA software package Autodesk Simulation Multi-physics®. In order to rank their severity and also to identify the presence of any interaction between main effects, a statistical analysis was performed on the results.

2. Method

Details of the full factorial experiment designed for this study shall first be discussed in section 2.1. For each of the treatment combinations (TC's) defined in our experiment design, a numerical fluid analysis was performed using a commercial software package (Autodesk Simulation CFD) as outlined in Section 2.2. This step was performed in order to quantify the flow rate through each fluid channel of the BIT array. With each fluid channel flow rate calculated, the thermal efficiency for each module of the BIT array was determined via the heat transfer analysis outlined in section 2.3. In this section we also provide detailed steps in the numerical approximation of the BIT fin efficiency using the finite difference method which takes into consideration the unique design of the BIT collector.

2.1 Experiment design

A two level full factorial (2^k) experiment was conducted so that the main and interaction effects of the four factors discussed in Section 1.0 could be identified. This experimental design was chosen in order to characterise all the variables under consideration including higher order interactions (Mathews, P. 2005). One major limitation of the full factorial experiment is that the size of the experiment is a function of the number of factors being

considered. However, as we are interested only in four factors, the total number of experiments of sixteen was deemed acceptable. Indeed it is stated elsewhere that a 2^k experiment is suitable when the number of factors is less than or equal to four (Antony, J. 2008). Designated labels and levels for each of the factors investigated are summarised in Table 1.

Table 1 Experiment factors and their levels.

Factor	Labels	Low level	High level
Manifold/Riser ratio	A	1	4
Array geometry	B	24	6
Direction of flow in manifold	C	Reverse	Parallel
Mass flow rate	D	0.0075 kg s^{-1} m^2	0.015 kg s^{-1} m^2

For Factor A, the manifold/riser ratio was varied between a low and high level of $\Phi_{manifold}/\Phi_{riser} = 1$ and $\Phi_{manifold}/\Phi_{riser} = 4$ respectively. A ratio of 1 was considered the lowest level by the authors, while a ratio of four was chosen to strike a practical balance between cost and performance. For Factor B, Array geometry was varied while maintaining a constant absorber area of 3.6 m^2. The array shape was adjusted by varying the number and length of BIT modules altering the aspect ratio of the BIT array. For the low level term, the array consisted of 24 BIT modules of length (L_{abs}) equal to 1 m. For the high level term, the array consisted of only six modules of L_{abs} = 4 m in length. The direction of flow in relation to the inlet/discharge manifolds (Factor C) as discussed in the previous section will have an effect on the flow distribution within the array. Factor C therefore is varied between reverse and parallel flow for the low and high levels respectively. Finally the mass flow rate, Factor D, is varied at the low level of $m = 0.0075$ kg s^{-1} m^2 and at the high level of $m = 0.015$ kg s^{-1} m^2.

The 2^k factorial experiment carried out was based on four factors (i.e. $k = 4$), providing a total of 16 treatment combinations. For each treatment combination, the corresponding factor levels are given in Table 2. The proceeding sections will discuss the method employed to computationally calculate the response of the system (η_{th}).

Table 2 Coded design matrix of experiment providing details of each of the 16 treatment combinations investigated.

TC	A	B	C	D
1	-1	-1	-1	-1
2	1	-1	-1	-1
3	-1	1	-1	-1
4	1	1	-1	-1
5	-1	-1	1	-1
6	1	-1	1	-1
7	-1	1	1	-1
8	1	1	1	-1
9	-1	-1	-1	1
10	1	-1	-1	1
11	-1	1	-1	1
12	1	1	-1	1
13	-1	-1	1	1
14	1	-1	1	1
15	-1	1	1	1
16	1	1	1	1

2.2 Fluid Analysis

A 2D planar analysis was performed using Autodesk Simulation Multi-physics to calculate the fluid velocities through each of the fluid channels of the BIT array. For our investigation, water was assumed to be the heat exchange fluid being actively circulated through the BIT array. As the water is being pumped through the collector, the effect of buoyancy was neglected.

Modelling only the fluid network, the mesh was generated automatically using four node quadrilateral elements operating under the Newtonian viscosity model. Two boundary conditions were specified for our simulation; a surface prescribed velocity at the inlet port of the fluid array which dictated the mass flow rate, and a free surface prescribed at the outlet port face (refer to Figure 2). Fluid velocity, *V* at the inlet port was calculated using Eq. (1).

$$m = \rho A V \qquad (1)$$

Where *m* is the desired mass flow rate (Factor D), *A* is the manifold area (m^2), and ρ is the density of water (kg/m^3).

The location of the outlet port for the array under study (Figure 2) was dependent on whether parallel or reverse flow direction was being analysed as directed by Table 2.
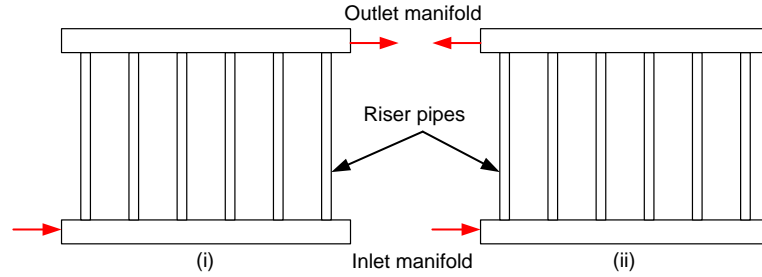

Figure 2 Diagram depicting the difference in flow connections of a header riser flow network for a parallel flow array (left) and a reverse flow array (right) (Ghani, F., Duke, M., et al. 2012).

Sixteen fluid simulations were conducted according to the treatment combinations listed in Table 2. For each simulation the fluid channel flow rates were taken and used for the heat transfer analysis.

2.3   Heat transfer analysis

Each treatment factor investigated in the previous section will result in a unique variation in absorber temperature due to the corresponding variation in fluid flow. The aim of our heat transfer analysis is to determine the thermal efficiency of each module in the BIT array followed by the calculation of the mean module thermal efficiency for each treatment factor. The absorber temperature distribution is calculated using Eq. (2) (Duffie, J.A. and Beckman, W.A. 2006).

$$T(x, y) = \frac{(T_b(y) - T_a - S/U_L)\cosh mx}{\cosh m(W - D)/2} + T_a + (S/U_L) \qquad (2)$$

Where T_b is the bond temperature, T_a is the ambient temperature, *S* is absorbed radiation (W/m^2), *x* represents an arbitrary distance perpendicular to fluid flow, *W* is the distance between tubes (m), *D* is the riser tube diameter (m), and U_L is the overall heat loss coefficient of the collector (W/m^2 K). The overall heat loss co-efficient for our unglazed collector was taken to be a constant value of 22 W/m^2 K (Anderson, T.N., Duke, M., et al. 2009) in our study. Variable *M* is calculated using Eq. (3).

$$M = \sqrt{\frac{U_L}{k\delta}} \qquad (3)$$

Where *k* is the thermal conductivity of the absorber material, and δ is the absorber plate thickness (m).

In order to solve Eq. (2), we must first calculate the bond temperature, T_b using Eq. (4) (Duffie, J.A. and Beckman, W.A. 2006).

$$T_b(y) = \frac{WF'\left[S - U_L(T_f(y) - T_a)\right]}{h_{fi}\pi D_i} + T_f(y) \qquad (4)$$

Where $T_f(y)$ is the temperature of fluid circulating through the collector, *F'* is the collector efficiency factor, and h_{fi} is the convective heat transfer coefficient. The fluid temperature will vary in the direction of flow and is therefore a function of *y* (m). The collector efficiency factor is calculated by (Duffie, J.A. and Beckman, W.A. 2006).

$$F' = \frac{1/U_L}{W\left[\dfrac{1}{U_L\left[D+(W-D)/F\right]} + \dfrac{1}{\pi D_i h_{fi}}\right]} \qquad (5)$$

Calculation of the collector efficiency factor requires the fin efficiency value *F*. Traditionally this value is determined by carrying out a classical fin analysis on the solar thermal absorber which is assumed to be a fin of rectangular cross section. Given the simple geometry of the classic fin, *F* is calculated by an analytical expression. However due to the structural ribs required to stiffen the building integrated collector as shown by Figure 3, such an analysis may lead to non-negligible error. To quantify this variation, the finite difference method was applied to calculate the temperature distribution and fin efficiency for a simplified version of the BIT collector under study.

2.3.1 Numerical calculation of fin efficiency

Geometry of the BIT collector for which the temperature distribution is to be calculated is shown in the bottom of Figure 3. As the collector is made from 2mm thick aluminium, a one dimensional steady state analysis was deemed sufficient for this investigation (as is the common practice in assessing fin performance (Incropera, F.P., DeWitt, D.P., et al. 2006)).
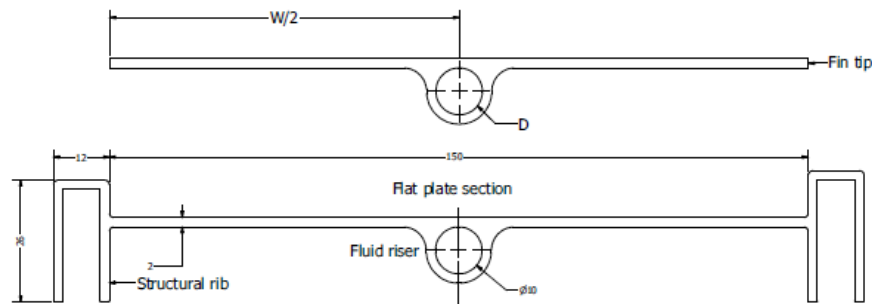

Figure 3 Comparison between the classical fin (top) and the simplified BIT collector designs.

A finite difference control volume analysis was performed for a nodal network structure illustrated in Figure 4. The structure modelled contained significantly more nodes employed than illustrated in Figure 7 and therefore the distance between each node (Δx) was sufficiently small. As the BIT collector was taken to be symmetrical about a vertical axis through the fluid channel, only half of the geometry was required for the simulation. The red arrows shown in Figure 5 indicate the nodes under radiation flux and the node under convection heat transfer (at the line of symmetry). As incidental radiation is assumed to be normal to the collector, only horizontal surfaces were exposed to radiation in this study. Irradiance, *G* was taken to be 1000 W/m². All nodes were subject to heat loss, q_{loss}.
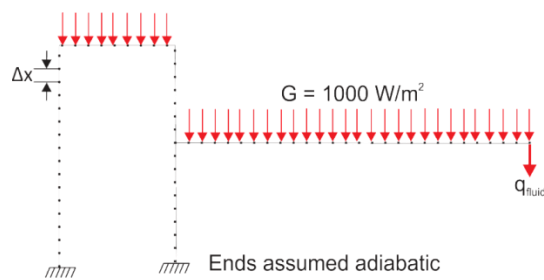

Figure 4 Nodal network of the BIT collector used to determine the temperature distribution using the finite difference method. Additionally, all nodes were subject to heat loss, q_{loss}.

The analysis consists of four nodal types; I) nodes under radiation flux, II) nodes under no radiation flux, III) node under convection heat transfer (i.e. node at fluid riser), and IV) adiabatic nodes at structural rib ends. A control volume analysis for each node type is presented in the following section.

2.3.1.1 Control volume analysis

Proceeding sections detail the control volume analysis for the nodes shown in Figure 7 operating under each set of boundary conditions. Both overall energy and finite difference equations are provided.

2.3.1.2 Node under radiation flux

Figure 6 below shows the node (*i*) and control volume (dotted box) of width Δx exposed to radiation.

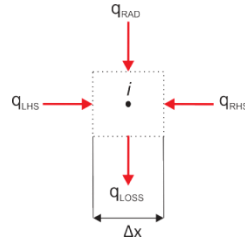**Figure 5** control volume for a node under incidental radiation.

A steady state energy balance yields,

$$q_{LHS} + q_{RHS} + q_{RAD} - q_{LOSS} = 0 \tag{2}$$

Where q_{LHS} and q_{RHS} represent conduction heat transfer with neighbouring nodes, q_{RAD} is radiation heat transfer to control volume, and q_{LOSS} represents heat loss to ambient. Substituting the relevant approximate rate equations (Fourier's Law) (Nellis, G. and Klein, S.A. 2009),

$$\frac{kA}{\Delta x}(T_{i-1} - T_i) + \frac{kA}{\Delta x}(T_{i+1} - T_i) + S\Delta x - U_L \Delta x (T_i - T_a) = 0 \tag{3}$$

Where S is the absorbed radiation (W/m^2) and U_L is the overall heat loss of the collector coefficient (W/m^2 ^{o}C). Procedure to calculate the overall heat loss coefficient will be presented in Section 2.2. As the collector panel length was assumed to be unity in the direction of fluid flow, the area A of the control volume perpendicular to conduction heat flux was taken to be equal to the value of fin thickness (δ). T_i represents the temperature of the node (and therefore the control volume), T_a is the ambient temperature, while T_{i-1} and T_{i+1} represent the temperature of nodes to the left and right respectively.

2.3.1.3 Node under no radiation flux
Figure 6 represents a control volume of the BIT collector under no radiation loading interacting with neighbouring nodes via conduction and heat loss to surroundings.
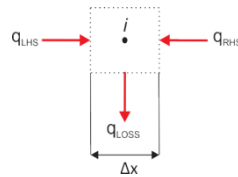
Figure 6 control volume for a node under no incidental radiation.

A steady state energy balance of the control volume shown by Figure 6 yields,

$$q_{LHS} + q_{RHS} - q_{LOSS} = 0 \tag{4}$$

$$\frac{kA}{\Delta x}(T_{i-1} - T_i) + \frac{kA}{\Delta x}(T_{i+1} - T_i) - U_L \Delta x (T_i - T_a) = 0 \tag{5}$$

2.3.1.4 Node under convection heat transfer
A single node (as indicated on the extreme right in Figure 7) is subject to both radiation and convective cooling due to fluid flow in the riser pipe in addition to conduction interaction with neighbouring nodes.
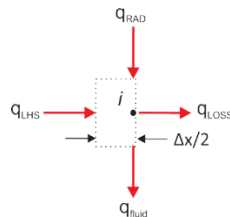
Figure 7 control volume for the node under incidental radiation and convective heat transfer.

An energy balance of the control volume shown by Figure 7 yields,

$$q_{LHS} + q_{RAD} - q_{LOSS} - q_{FLUID} = 0 \tag{6}$$

$$\frac{kA}{\Delta x}(T_{i-1} - T_i) + \frac{\Delta x}{2}S - \frac{\Delta x}{2}U_L(T_i - T_a) - \frac{h_{fi}\pi D}{2}(T_i - T_f) = 0 \tag{7}$$

Where T_f is the fluid temperature, D is the riser pipe diameter (m), and h_{fi} is the forced convection heat transfer coefficient(W/m^2 K) calculated by (Incropera, F.P., DeWitt, D.P., et al. 2006),

$$h_{fi} = \frac{Nuk}{D} \tag{8}$$

For a circular tube, the Nusselt number Nu is independent of velocity for laminar flow conditions but is dependent on the thermal boundary condition (Incropera, F.P., DeWitt, D.P., et al. 2006). The value can be taken as either 4.36 and 3.66 for uniform surface heat flux and constant wall temperature conditions respectively (Incropera, F.P., DeWitt, D.P., et al. 2006). In this work we assumed a Nusselt number of 4.36. For $T_f = 20^{\circ}$C, the thermal conductivity value k was taken to be 0.6 W/m K (Duffie, J.A. and Beckman, W.A. 2006). For a pipe 0.01m in diameter, the heat transfer coefficient h_{fi} was calculated to be 260 W/m^2 K.

2.3.1.5   Nodes at adiabatic boundary conditions
The ends of the roof ribs were assumed to be adiabatic as indicated in Figure 4. For the control volume shown in Figure 8, only two energy flows are presented q_{LHS} and q_{LOSS} representing conduction with its neighbouring node and heat loss to ambient respectively. The energy balance and finite difference equations were determined to be,
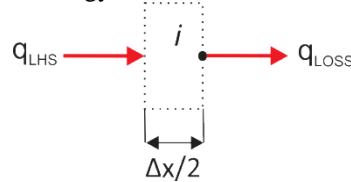

Figure 8 control volume for the nodes at rib ends.

$$q_{LHS} - q_{LOSS} = 0 \tag{9}$$

$$\frac{kA}{\Delta x}(T_{i-1} - T_i) - \frac{\Delta x}{2}U_L(T_i - T_a) = 0 \tag{10}$$

2.3.1.6   Calculation of the overall heat loss coefficient
In the analysis of solar thermal systems, it is useful to represent heat losses from the collector to its surroundings using an overall heat loss coefficient U_L in order to simplify the mathematics behind the analysis. The overall heat loss coefficient is the summation of heat losses experienced from the collector's top, edges, and bottom surfaces (Duffie, J.A. and Beckman, W.A. 2006).

Given the unique design of the collector under study were it is integrated directly into the building envelope without a top cover, the procedure for calculating U_L will vary somewhat from that of a traditional solar thermal collector. Anderson et al. (Anderson, T.N., Duke, M., et al. 2009) determined the overall heat loss coefficient to be 22 W/m^2 K for an unglazed building integrated PV/T collector very similar to the one considered in this study. This value was obtained considering that the building integrated collector is installed above an air-filled, triangular, enclosed attic in which the trapped air essentially acted as a layer of insulation. The value calculated for U_L obtained Anderson et al. was used for our study.

2.3.1.7   Calculation of temperature distribution *T(x)*
For *N* nodes, an *N* number of finite difference equations were developed based on the control volume analysis discussed in previous sections in order to determine *N* unknown temperatures. Finite difference equations presented in sections 2.11, 2.12, 2.13, and 2.14 were modified to fit the following matrix equation format (Myers, G.E. 1987):

$$\underline{A}\,\underline{X} = \underline{b} \tag{11}$$

Where $\underline{A}$ is a sparse-type matrix consisting of the unknown temperature coefficients, $\underline{X}$ is the vector of unknown temperatures to be found, and $\underline{b}$ is a vector of the corresponding constant terms for each control volume.

Using Matlab® software, matrix $\underline{A}$ and vector $\underline{b}$ were compiled using the finite difference equations previously discussed. The linear system of *N* equations was solved using Gaussian Elimination to obtain vector $\underline{X}$ of unknown temperatures. A comparison of the temperature distribution is made in Figure 9 between the BIT collector and a

traditional flat plate collector. We can see at $x = 0$, the temperature of the BIT collector is somewhat lower due to additional heat losses through the ribs. Based on these results we can expect a reduction in the fin efficiency value of the BIT collector.
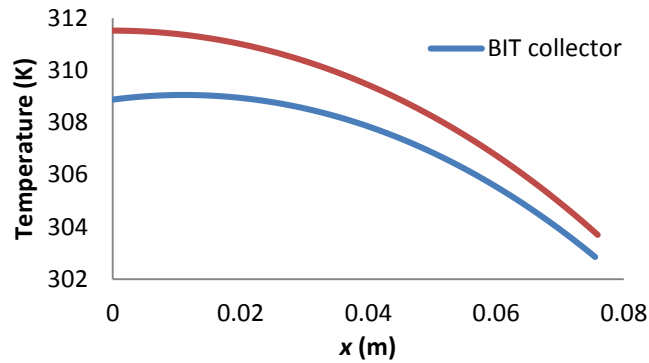

Figure 9 Temperature distribution for the BIT collector along the fin compared with the temperature distribution of a standard flat plate collector. Both sets of data were calculated numerically using the finite difference method.

2.3.1.8 Calculation of fin efficiency *F*
The fin efficiency for a straight fin with a rectangular profile under uniform radiation is calculated using Eq. (12). This equation is typically used for the analysis of the traditional flat plate solar thermal collector.

$$F = \frac{\tanh[m(W-D)/2]}{m(W-D)/2} \tag{12}$$

The calculation of the fin efficiency value depends on the boundary condition at the fin tip and the geometry of the fin. Eq. (12) assumes a straight, rectangular geometry and hence would not yield an accurate value for the BIT collector fin which must, therefore, be calculated numerically. The fin efficiency is defined as the ratio of the heat transfer away from the actual fin to the heat transfer away from an ideal fin (Nellis, G. and Klein, S.A. 2009)).

The energy conducted to the region of the fluid riser can be determined using Fourier's law. Using Eq. (13) below, the finite difference method is used to calculate conduction heat transfer through the fin above the riser. Where T_N represents the temperature of node N (at fluid riser) and T_{N-1} is the temperature of the adjacent node.

$$q'_{fin} = -k\delta \frac{dT}{dx}\bigg|_{x=\frac{(W-D)}{2}} = k\delta \frac{T_{N-1} - T_N}{\Delta x} \tag{13}$$

The value obtained using Eq. (13) was multiplied by two as the value obtained using Eq. (13) represents conduction from one side of the riser tube only. The heat transfer value for the ideal fin was numerically calculated by setting the thermal conductivity of the fin to infinity.

$$F_{BIT} = \frac{q'_{fin}}{q'_{ideal}} \tag{14}$$

Inspecting Figure 9 we can see that the fin edge temperature for the BIT collector is lower compared to the values obtained using Eq. (1) due to conduction losses through the structural ribs. For the BIT collector, we numerically determined the fin efficiencies to be 0.88 while the fin efficiency for a traditional flat plate collector of equivalent characteristics was found to be 0.93, which represents a 5.2% drop in fin efficiency.

2.3.2 Module efficiency calculation
Fluid temperature for each riser, $T_f(y)$ needed for Eq. (6) is calculated by Eq. (15) (Duffie, J.A. and Beckman, W.A. 2006).

$$T_f(y) = (T_{fi} - T_a - S/U_L)e^{\left(\frac{-U_L W F' y}{\dot{m} C_p}\right)} + T_a + S/U_L \tag{15}$$

The process of calculating the absorber temperature, $T(x, y)$ begins by initially estimating a value for the mean fluid temperature (T_{fm}) so that fluid properties such as viscosity (μ_f), thermal conductivity (k) and Prandtl number (Pr) can be interpolated from tabulated data. The mean fluid temperature (T_{fm}) is calculated by Eq. (16).

$$T_{fm} = \frac{T_{fo} + T_{fi}}{2} \tag{16}$$

Where T_{fo} and T_{fi} represent the values of outlet and inlet fluid temperature respectively. In our study, the inlet fluid temperature, T_{fi} was kept constant at 20 °C. The outlet fluid temperature is found using Eq. (15) with y set to the length of the absorber.

Using the riser mass flow rates determined in our fluid flow analysis, the Reynolds number (Re_D) was calculated using Eq. (17) with the assumption that flow was steady and incompressible and within a pipe of uniform cross sectional area (Duffie, J.A. and Beckman, W.A. 2006).

$$\mathrm{Re}_D = \frac{4\dot{m}}{\pi D \mu} \tag{17}$$

Where D is the diameter of riser pipe and μ is fluid viscosity. For values of $Re_D < 2300$, flow was considered laminar and fully developed. Conservative heat transfer coefficient values was calculated by making the constant wall temperature assumption (Duffie, J.A. and Beckman, W.A. 2006). Here, the Nusselt number (Nu) was taken to be 3.66 (Kays, W.M. and Crawford, M.E. 1993). The convective heat transfer coefficient (h_{fi}) of fluid circulating in the riser may then be calculated by re-arranging Eq. (15).

$$Nu = \frac{h_{fi} D}{K} \tag{15}$$

Once the convective heat transfer coefficient, h_{fi} was found, the fin efficiency factor, F' and fluid temperature, $T_f(y)$ were calculated. With the new value of outlet fluid temperature found, the new value for mean fluid temperature, $T_{fm,i+1}$ was calculated using Eq. (16) and compared to the previous value of $T_{fm,i}$. The process of calculating F' and T_{fo} was repeated until the error in subsequent iterations was within a user specified tolerance. Final values of F' and T_f were then used to calculate the bond temperature (T_b) and absorber temperature (T) using Eq. (6) and Eq. (4) respectively. This process was repeated in Matlab for each of the 16 treatment combinations. Finally once T_{fo} was found, the useful energy gain, Q_u was calculated using Eq. (16)

$$Q_u = mC_p(T_{fo} - T_{fi}) \tag{16}$$

Where m is the riser mass flow rate (calculated from our fluid analysis), and C_p is the specific heat of water (kJ/kg K). The thermal efficiency (η_{th}) can now be calculated using Eq. (17) for each module. All module efficiency values were then averaged to give the final array response.

$$\eta_{th} = \frac{Q_u}{GA_c} \tag{17}$$

3. Results and Discussion

The objective of our analysis was to determine the ranking of the main effects and identify any significant secondary interactions. To achieve this aim a statistical analysis was carried out on the data collected from all treatment combinations investigated. An analysis of variance (ANOVA) study was carried out using Minitab 16 software.

Figure 10 illustrates the Pareto plot (Mathews, P. 2005) of main effects and secondary interactions. Higher order interactions were found to be insignificant and systematically removed in our study. The graph shows that all four main effects are significant at the 5 per cent significance level (i.e. $\alpha = 0.05$). Geometry of the array was shown to have greatest effect on the thermal efficiency followed by the manifold to riser ratio, mass flow rate, and the direction of flow in the manifolds. Interestingly we can see that in addition to the main effects, there is a strong interaction between the array geometry (Factor B) and the direction of flow in the manifold (Factor C), and also between the manifold to riser ratio (Factor A) and array geometry (Factor C). These results identify the need in the appropriate selection of the manifold to riser channel ratio and the direction of flow in the manifolds for a BIT collector of specified geometry.
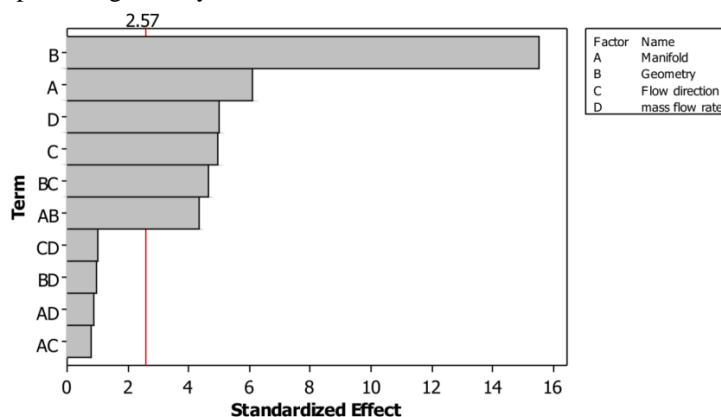

Figure 10 Pareto plot of effects at 5 per cent significance level.

4. Conclusion

In our study a two level full factorial experiment was designed to determine what effect four design factors and their interactions will have on the thermal efficiency of a building integrated thermal collector. A computational analysis was performed in order to approximate the fluid flow and corresponding temperature distribution of each of the 16 treatment combinations using a commercial FEA package and Matlab software. Furthermore, a numerical analysis was conducted to quantify the fin efficiency of a BIT collector using the finite difference method which revealed the BIT collector will suffer a 5% drop in fin efficiency due to additional fin tip heat losses through the structural ribs of the collector. From these results the thermal efficiency values were calculated for each module and averaged for each treatment factor. A statistical analysis revealed that the array geometry will have the strongest influence, followed by the manifold to riser channel ratio, mass flow rate, and lastly the direction of flow in the manifold (i.e. parallel or reverse flow). Two secondary interactions were also found to be statistically significant at 5 per cent significance level. The array geometry and direction of flow in the manifold followed by the array geometry and the manifold to riser channel ratio interactions will both affect the thermal yield of a BIT collector. The authors believe the research presented is valuable to those responsible in the design of BIT systems.

5. References

Anderson, T.N., Duke, M., Morrison, G.L. and Carson, J.K. 2009 Performance of a building integrated photovoltaic/thermal (BIPVT) solar collector. *Solar Energy*, **83**, 445-455.

Antony, J. 2008 *Design of experiments for engineers and scientists*. Butterworth-Heinemann, Oxford.

Asif, M. and Muneer, T. 2007 Energy supply, its demand and security issues for developed and emerging economies. *Renewable and Sustainable Energy Reviews*, **11**, 1388-1413.

Chiou, J.P. 1982 The effect of nonuniform fluid flow distribution on the thermal performance of solar collector. *Solar Energy*, **29**, 487-502.

Corbin, C. and Zhiqiang, J.Z. 2010 Experimental and numerical investigation on thermal and electrical performance of a building integrated photovoltaic-thermal collector system. *Energy and Buildings* **42**, 76-82.

Duffie, J.A. and Beckman, W.A. 2006 *Solar engineering of thermal processes*. 3rd edn. John Wiley & Sons, New Jersey.

Ghani, F., Duke, M. and Carson, J.K. 2012 Effect of flow distribution on the photovoltaic performance of a building integrated photovolatic/thermal (BIPV/T) collector. *Solar Energy*, **86**, 1518-1530.

Incropera, F.P., DeWitt, D.P., Bergman, T.L. and Lavine, A.S. 2006 *Fundamentals of Heat and Mass Transfer*. John Wiley & Sons, New York.

Jones, G.F. and Lior, N.L. 1994 Flow distribution in manifold solar collectors with negligible buoyancy effects. *Solar Energy*, **52**, 289-300.

Kays, W.M. and Crawford, M.E. 1993 *Convective Heat and Mass Transfer*. 3rd ed. edn. McGraw-Hill, New York.

Mathews, P. 2005 *Design of experiments with Minitab*. ASQ Quality Press, US.

Medved, S., Arkar, C. and Cerne, B. 2003 A large-panel unglazed roof-integrated liquid solar collector-energy and economic evaluation. *Solar Energy*, **75**, 455-467.

Myers, G.E. 1987 *Analytical methods in conduction heat transfer*. Genium Publishing Corp, US.

Nellis, G. and Klein, S.A. 2009 *Heat Transfer*. Cambridge University Press, New York.

Wang, S.A. and Wu, L.G. 1990 Analysis and performance of flat-plate solar collector arrays. *Solar Energy*, **45**, 71-78.

Weiss, W. and Mauthner, F. 2012 Solar heat worldwide markets and contributions to the energy supply 2010. *Solar Heating & Cooling Programme*, International Energy Agency.

Zhai, X.Q., Wang, R.Z., Dai, Y.J., Wu, J.Y., Xu, Y.X. and Ma, Q. 2007 Solar integrated energy system for a green building. *Energy and Buildings*, **39**, 985-993.